Int. J. Heat Mass Transfer. Vol. 27, No. 6, pp. 815–827, 1984
Printed in Great Britain

0017–9310/84 $3.00 + 0.00
Pergamon Press Ltd.

SIMULATION OF THE VERTICAL FLOW OF A THIN, WAVY FILM USING A FINITE-ELEMENT METHOD

POUL BACH and JOHN VILLADSEN*
Instituttet for Kemiteknik, Danmarks Tekniske Højskole, Lyngby, Denmark

(*Received* 1 *October* 1982 *and in revised form* 9 *May* 1983)

Abstract—The Navier–Stokes equations for a two-dimensional liquid film which is drained down a vertical wall in laminar flow are formulated in terms of the Lagrangian velocities and solved by a finite-element method. Excellent agreement is obtained between simulated results for wave celerity and wave form, and the corresponding experimental results. The momentum and mass balances, discretized in terms of the nodal point values for the velocities and the pressure, are solved by Galerkin's method. To avoid distortion of the network for increasing integration time a rezoning procedure has been developed. This overcomes a major deficiency of the Lagrangian formulation, and allows integration to proceed until a stationary wave profile is reached.

NOMENCLATURE

$2A$	height of the wave peak (see Fig. 6)
B	breadth of initial perturbation
A, C, D, E, F	Galerkin matrices defined in equation (14) and in the Appendix
c	travelling speed (celerity) of the large wave
g	acceleration of gravity (982 cm s^{-2})
$h(x, t)$	distance from wall to free surface of liquid, h
h_N	Nusselt film thickness, $(3Q\mu/\rho g)^{1/3}$
h_{mx}	maximum distance from wall to wave surface (Fig. 6)
h_G	height of initial perturbation
$2H$	mean curvature of liquid surface
L_b, L_f	shape factors for wave (Fig. 6)
N_x, N_y	number of elements in x- and y-direction, respectively
p	pressure at point P in the liquid film
P	vector of pressures at nodal points
q	parameter defined in equation (19)
Q	volumetric flow per unit wetted perimeter ($cm^2\ s^{-1}$)
Re_N	Reynolds number for liquid film, $4Q\rho/\mu$
t	an arbitrary time after initiation of the liquid flow at t_0
(u, v)	components of liquid velocity at point P in the liquid, defined in equation (1)
$\langle u_N \rangle$	average linear velocity for Nusselt flow, Q/h_N
U_N	surface velocity of Nusselt film with thickness h_N, $1.5\langle u_N \rangle$
U_h	surface velocity of Nusselt film with thickness $h(x)$
V	vector of velocities at nodal points, defined in equation (13)
$\mathbf{V}_1$	reordered velocity vector defined in equation (A4)
(x, y)	Eulerian coordinates (Fig. 1)
(x_n, y_n)	nodal point coordinates in an element.

Greek symbols

μ	viscosity of liquid
(ξ, η)	local coordinate of point P in the element
ρ	density of liquid
σ	surface tension of liquid
ϕ_n, ψ_n	interpolation functions for the velocity and the pressure field in an element. Defined in equations (10) and (11)
Ω	area of an element.

INTRODUCTION

THE FLOW of thin liquid films occurs in a variety of process equipment including falling film evaporators, wetted wall absorbers and chemical reactors. Almost all experimental investigations report the presence of a wavy interface of apparently complicated form. Large waves slide rapidly down over a thin liquid substrate, and a large part of the total mass of the film appears to be carried by these waves which are often far enough apart to be regarded as solitary waves. In between the large waves the substrate is covered by a fine wave structure with wave amplitudes of only a fraction of the substrate thickness. The liquid side mass transfer is heavily influenced by the large waves while the small waves may contribute significantly to the gas side transfer processes.

In order to improve the performance of film type mass and heat transfer equipment it becomes highly desirable to calculate the variation of local transfer coefficients with the properties of the liquid phase. As a necessary preliminary to these calculations the velocity and pressure field in the film must be simulated. Here the development of the wavy surface structure of the

* Also: Department of Chemical Engineering, University of Houston, Houston, TX 77004, U.S.A.

film and its influence on the velocity field is of particular interest.

The mathematical model for the velocity and pressure field of the wavy liquid film is, however, exceedingly complicated, and despite numerous efforts over the last 20 years no rigorous numerical solution has been accomplished. The model approximations which are customarily made before starting the numerical solution are not always quite satisfactory, and in particular the way in which the boundary conditions at the free surface are treated leaves much to be desired.

The wavy film is simulated by an extension of the numerical method which has recently been introduced by Bach and Hassager [1]. We shall mainly be concerned with a description of the method, whereas a more complete comparison between simulated and available experimental results will be given elsewhere. A few recent experimental investigations will, however, be quoted since they contain certain results which can immediately be compared with our simulations. The three examples at the end of the paper show that excellent agreement is obtained between simulated and experimental results for certain key parameters of the wave structure.

Brauner and Maron [2, Fig. 4] report a large increase in the local wall to liquid mass transfer coefficient just as the wave front passes the measurement probe—a clear indication that the disturbance of the velocity field which is caused by the large waves penetrates to the bottom of the film. The ratio between celerity c of the waves and the Nusselt average linear velocity $\langle u_N \rangle$ is shown [2, Fig. 13] to decrease rapidly with increasing film Reynolds number Re_N in the range $0 < Re_N \gtrsim 100$, while approaching an asymptotic value of ~ 1.55 for $Re_N > 1000$. The waves develop at some distance D from the top of the falling film, first as small ripples which later grow into the final wavy structure where the mass carrying waves may have an amplitude several times as large as the substrate thickness. The distance D seems to increase slowly when Re_N increases, while addition of surfactants drastically increases D with the result that the experimental equipment may become too short to allow the wave structure to develop, as discussed by Strobel and Whitaker [3].

Nakorykov *et al.* [4, 5] shows oscillograms of the large ('rolling' in their nomenclature) waves. The amplitude of the waves increases with increasing Re_N, and a damped harmonic wave structure is observed in front of the wave when $Re_N \gtrsim 50$–100. This capillary type 'forerunner' wave structure is also observed by Pierson and Whitaker [6], and it is reported in the classical papers of Kapitza [7, p. 708].

The waves grow from initial perturbations of the film thickness, and since these perturbations may occur at random intervals it may well happen that the solitary waves are not observed in some experimental studies. Especially if the large wave is preceded by a capillary forerunner wave, which may overlap another large wave, the resulting wave structure can become so complicated that it appears to be random, as discussed in Telles and Dukler [8] and in Chu and Dukler [9, 10].

MATHEMATICAL MODEL FOR A TWO-DIMENSIONAL (2-D) INCOMPRESSIBLE FILM

Figure 1 shows the 2-D film which flows down a vertical wall at $y = 0$ under the influence of gravity.

Let the Lagrangian velocity field (u, v) be defined by

$$\frac{\partial x}{\partial t} \equiv u \quad \text{and} \quad \frac{\partial y}{\partial t} \equiv v, \tag{1}$$

where x and y determine the position at time t of a fluid particle which was located at (x_0, y_0) at time $t = t_0$.

The x and y momentum balances and the mass balance for the flowing liquid are stated in equations (2)–(4)

$$\rho \frac{\partial u}{\partial t} = \rho g - \frac{\partial p}{\partial x} + \mu \left(\frac{\partial^2 u}{\partial x^2} + \frac{\partial^2 u}{\partial y^2} \right), \tag{2}$$

$$\rho \frac{\partial v}{\partial t} = - \frac{\partial p}{\partial y} + \mu \left(\frac{\partial^2 v}{\partial x^2} + \frac{\partial^2 v}{\partial y^2} \right), \tag{3}$$

$$\frac{\partial u}{\partial x} + \frac{\partial v}{\partial y} = 0. \tag{4}$$

The non-linear convective terms which appear in the Eulerian formulation of the momentum balances are absent in the Lagrangian formulation (see Lamb [11, p. 12] for an inviscid fluid and Connor and Brebbia [12, p. 301] for the full equations (1)–(4)).

At the wall the velocity field is specified by

$$u = v = 0 \quad \text{at} \quad y = 0, \tag{5}$$

while a stress balance normal to the free surface, equation (6), and tangential to the free surface, equation (7), provide the remaining boundary conditions at $y = h(x, t)$

$$\tau_{nn} + p = 2H\sigma, \tag{6}$$

$$\tau_{ns} = 0, \tag{7}$$

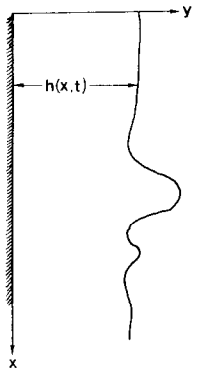

FIG. 1. The wavy liquid film with thickness $h(x, t)$ at position x and time t.

where $2H$ is the mean curvature of the free surface

$$2H \equiv \frac{\partial^2 h}{\partial x^2}\left(1+\left(\frac{\partial h}{\partial x}\right)^2\right)^{-3/2}. \tag{8}$$

In equation (7) we assume that there is no gas flow, and hence that there is no surface shear stress. The pressure outside the interface is assumed to be zero.

Equations (1)–(4) constitute a set of five partial differential equations which describe the time change of position, velocities and pressure of a fluid particle, originally located at (x_0, y_0) and with velocities (u_0, v_0). Equations (5)–(7) yield the boundary conditions for the fluid mechanical equations.

FINITE-ELEMENT METHOD FOR SOLUTION OF THE MODEL

Following Bach and Hassager [1] the liquid volume originally contained within ($x = 0$, $x = x_{max}$), ($y = 0$, $y = h(t = t_0, x)$) is discretized into a quadrilateral element network with N_x elements in the x-direction and N_y elements in the y-direction. Each element is defined by the position of the nodal points, and the number of nodal points varies with the degree of the element. Bach and Hassager [1] used elements with linear sides where the four corners are used as nodes. We shall use quadratic 2-D elements where the sides are parabolas. Eight nodal points are necessary to describe the geometry of the quadratic element, and these are chosen as the four corners and the midpoints of the parabolic sides. The quadratic element with its original rectangular shape at $t = t_0$ is shown in Fig. 2(a). In the local (ξ, η) coordinate system of the element the corner nodes 1, 3, 5 and 7 are at $(-1, -1)$, $(1, -1)$, $(1, 1)$ and $(-1, 1)$. At some later time t the element has been distorted into the shape shown in Fig. 2(b), but its area Ω is unchanged when the fluid is incompressible. A fluid particle P which flows with the liquid retains its local coordinates (ξ_P, η_P) after the distortion of the element.

We shall use isoparametric elements [13, p. 81] for which the variation of an unknown function (here the velocity field) is computed from function values at the nodal points by the same set of interpolation functions as are used to compute the position of a given point within the element. Consequently, at any given time when the nodal coordinates of the quadratic element are (x_n, y_n) one may use the interpolation formula (9) to calculate the Eulerian coordinates (x, y) which correspond to given local coordinates (ξ, η)

$$(x, y) = \left(\sum_1^8 \phi_n(\xi, \eta)x_n, \sum_1^8 \phi_n(\xi, \eta)y_n\right). \tag{9}$$

Correspondingly, for the isoparametric quadratic element

$$(u, v) = \left(\sum_1^8 \phi_n(\xi, \eta)u_n, \sum_1^8 \phi_n(\xi, \eta)v_n\right). \tag{10}$$

It has been known for some time (see Sani *et al.* [14] for a detailed discussion) that FEM simulation of the Navier–Stokes equations, especially when generated by Galerkin's method, will run into serious numerical difficulties if equal order approximations are used for the velocity and pressure fields. In general, a lower order approximation must be used for the pressure field, and we take the pressure to vary bilinearly within the element. Since we want to keep the number of nodal points to a minimum we choose to let the quadrilateral bilinear element pass through the corner nodes of the quadratic element in Fig. 2 (the midpoint nodes 2, 4, 6 and 8 could also have been used). On Fig. 2(b) we show the distorted bilinear element by broken lines.

Consequently, the pressure is calculated by the four point interpolation formula

$$p = \sum_1^4 \psi_n(\xi, \eta)p_n. \tag{11}$$

The isoparametric interpolation functions ϕ_n and ψ_n are listed in the Appendix for the elements which we have used [13, p. 83].

Within the element u, v and p are approximated by the 2-D polynomial functions (10) and (11). These are inserted into the momentum and mass balances (2)–(4) and, following the principle of Galerkin's method, the residuals (Res) are made orthogonal over the element area Ω on the trial functions ϕ_n and ψ_n, respectively to give a set of equations for the nodal point values of u, v and p (see Chung [13, p. 207] for a discussion of the choice of trial functions ϕ_n in equation (12) and ψ_n in equation (13))

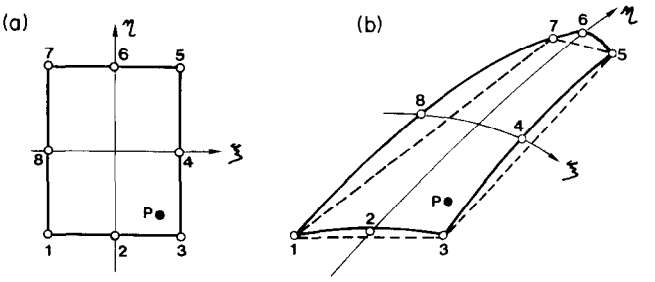

FIG. 2. Quadratic element at time t_0 and after distortion at time t. The bilinear element is shown with broken lines on FIG. 2(b).

Equations (2) and (3):

$$\int_\Omega \text{Res} \cdot \phi_n \, d\Omega = 0, \quad n = 1, 2, \ldots, 8, \quad (12)$$

Equation (4):

$$\int_\Omega \text{Res} \cdot \psi_n \, d\Omega = 0, \quad n = 1, 2, 3, 4. \quad (13)$$

Since the velocities u and v are each represented by eight nodal point values and the pressure by four nodal point values, equations (12) and (13) form a set of 20 equations in $\mathbf{V} = (u_1, u_2, \ldots, u_8, v_1, v_2, \ldots, v_8)$ and $\mathbf{P} = (p_1, p_2, p_3, p_4)$.

The final form of the Galerkin equations is

$$\mathbf{DV} - \mathbf{CP} = -\mathbf{A}\frac{d\mathbf{V}}{dt} + \mathbf{F} + \mathbf{E}, \quad (14)$$

$$\mathbf{C}^T\mathbf{V} = 0. \quad (15)$$

In the derivation of equations (14) and (15) the Green–Gauss theorem has been used to eliminate terms with second-order derivatives of the trial functions [13, p. 42], a device which leads to a considerable simplification in setting up the equations.

The surface term **E** appears only in those elements which adjoin the free surface. **D** and **A** are (16×16) matrices, **C** is a (16×4) matrix, and $\mathbf{C}^T$ is the transpose of **C**. The elements of **A**, **C**, **D**, **E** and **F** all depend on the values of x and y at the current time step, and consequently the solution of equations (14) and (15) is coupled to the time change of the nodal point coordinates (x_n, y_n) via the solution of equation (1), discretized by means of equation (9).

In order to avoid errors in the computer program a very systematic approach must be used to set up the matrices and vectors in equations (14) and (15). The explicit expressions in the Appendix may be of considerable help in this respect.

The individual element equations are finally coupled together to give a global set of equations for all nodal points in the network. This global set of equations is integrated one step forward in the t-direction. Since the dimension of the system is enormous an extremely simple, yet stable integration method should be used. A predictor–corrector approach seems to be the best: from the previous (or several previous) integration step(s), values of (x_n, y_n) for all points in the network are obtained by extrapolation to the current time step $t + \Delta t$. Now **A**–**F** in equations (14) and (15) can be constructed for each element, and the global set of network equations which is linear in **V** and **P** can be solved at $t + \Delta t$ using $d\mathbf{V} \sim \mathbf{V}_{t+\Delta t} - \mathbf{V}_t$ and $\mathbf{V} = \mathbf{V}_{t+\Delta t}$, $\mathbf{P} = \mathbf{P}_{t+\Delta t}$.

Next the discretized version of equation (1) is integrated with $\mathbf{V} = \frac{1}{2}(\mathbf{V}_t + \mathbf{V}_{t+\Delta t})$, and **A**–**F** are updated. Starting with a small Δt the iterations are made to converge in two or three steps, and a cautious policy of increasing Δt can be implemented. Δt should, however, not be increased so rapidly that more than four or five iterations are necessary, since this inevitably leads to a waste of computer time.

Whereas the boundary conditions on y are built into the formulation of the finite-element approximation, it has not up to this point been necessary to define the initial conditions $(u_n, v_n, h(x))$ at time t_0, and the inlet and exit boundary conditions on x.

We have chosen an initial condition with $(u_n, v_n) = 0$ at $t = t_0$ and $h = h_N$, the Nusselt film thickness. For $t > t_0$, $v = 0$ at the inlet $x = 0$ while u builds up to the Nusselt velocity profile as is described for an analogous example in Bird *et al.* [15, p. 125].

There is no doubt that the knitting together of all the element equations is the crucial step of the FEM simulation—not only to avoid formal errors, but also to achieve an efficient computer code. Chung [13, p. 43] gives an outline of a code in Boolean algebra, but each individual FEM simulator probably uses its own methodology. Our complete code is listed in Bach [16].

We shall next discuss the total dimension of the system of equations and how this dimension can be reduced. Furthermore, some remarks will be given on the required size of N_x and N_y, the number of elements in the x- and y-directions, respectively.

With our quadratic elements for the geometry and the velocity field and with linear elements for the pressure field the total number of equations in **V** and **P** is

$$N = \underbrace{2[(3N_x + 2)N_y + 2N_x + 1]}_{\text{(equations for } u \text{ and } v)} + \underbrace{(N_x + 1)(N_y + 1)}_{\text{(pressure field)}}. \quad (16)$$

We have used equation (5) to eliminate u and v at the boundary $y = 0$ before solving the global equations. This device is easily implemented and it automatically leads to a reduction of N by $2(2N_x + 1)$ equations to give

$$N = 2(3N_x + 2)N_y + (N_x + 1)(N_y + 1). \quad (17)$$

The required value of N_y depends on the rate of variation of the properties over the thin film. If $N_y = 1$ the elements become severely distorted since their lower edge is fixed due to the no slip boundary condition at $y = 0$ while the upper edge moves with the surface velocity. The variation of the variables over the element becomes difficult to approximate with sufficient accuracy and $N_y \geqslant 2$ is recommended. Our simulations do, however, show that there is very little difference between results obtained with $N_y = 2$ or 3. In other problems—e.g. if mass transfer from the wall is to be studied—it may become necessary to include more elements close to the wall, but to compute the velocity field we believe that $N_y = 2$ is almost always sufficient.

The value of N_x is determined by the length to amplitude ratio of the wave structure to be studied. Typical values of about 100 for this ratio are reported by Dukler [17], which would suggest $N_x \approx 100$. The rezoning procedure to be described in the next section does, however, to a considerable extent eliminate the need for a large N_x since very thin elements are automatically produced by the algorithm in those

regions where dramatic changes in the velocity field occur. For $Re_N < 100$ we have obtained a very satisfactory accuracy with $N_x = 25$ and the automatic rezoning procedure.

One final comment is appropriate concerning the assumption that for an incompressible liquid the area Ω of each element should remain constant during the transformation of the network. This is, of course, implied by the continuity equation (4), but when this is discretized by the Galerkin approximation (13) continuity cannot be expected to hold exactly. Furthermore, a somewhat non-standard Galerkin method is used in equation (13) since the residual consists of ϕ_n, $\partial\phi_n/\partial x$ and $\partial\phi_n/\partial y$ and it is made orthogonal on ψ_n which belongs to another set of trial functions. As a result of the approximations the numerical calculations show that the elements are slightly compressed in regions where the pressure is high. This obviously gives rise to some error in the local velocities, but since these change rapidly in regions where the pressure becomes significantly larger than zero, it is certainly very difficult to get experimental values of v and u with an accuracy which is even approximately equal to that of the simulated values. We have estimated that errors in v and u of about 6–10% may result in the forefront of the wave where the compression of liquid elements is most pronounced. Experimental values of u and v could hardly be found with more than $\sim 50\%$ accuracy in this region.

LOCATION AND REZONING PROCEDURES

When the element network equations are solved in a coordinate system which moves with the fluid particles the determination of the film thickness $h(x, t)$ causes no problems. The values of y_n, v_n and u_n for the $\eta = 1$ edge of the uppermost finite elements in the network directly yield the form of the free surface and the components of the velocity vector at the film surface. This is in sharp contrast with the Eulerian formulation of the finite-element equations where the complicated surface boundary conditions lead to extraordinary numerical difficulties—which are hard to circumvent without making more or less justified model approximations. In this context the inconvenience of having to integrate equations (1) in parallel with the fluid mechanical equations (2)–(4) hardly detracts anything from the virtues of the Lagrangian description.

There are many fluid mechanical studies where FEM is applied with an Eulerian description of the system [18–20]. In other problems the Lagrangian formulation has been used successfully. The first papers on Lagrangian FEM by Hassager and coworkers are particularly relevant [1, 21].

The major difficulty with the application of a Lagrangian FEM to the wavy film problem is that the elements become severely distorted when the coordinate system moves with the liquid, while they retain their original shape in the Eulerian coordinates. The no slip boundary conditions at the wall fix the position of the $\eta = -1$ edge of the bottom elements while nodal points closer to the free surface move progressively faster due to the increase of u with y. Even for small values of Re_N the elements rapidly become very elongated and the interpolation functions gradually lose their ability to interpolate accurately within the element as shown by Oden [22] in an early paper on FEM. Finally, when the sides of the element are about to cross each other (det (J) in equation (A13) becomes zero) the network breaks down.

Another, but far less serious problem, inherent in the Lagrangian formulation is that of finding u, v and p at a fixed position (x, y) as a function of time. This location problem must be solved as a preliminary to the periodical reconstruction of the finite-element network which will be proposed as a remedy for the loss of accuracy due to distortion of elements.

The location problem consists of two parts. For any given time t it is desired to determine:

(1) the element E_t in which a fixed point P $= (x, y)$ is located;

(2) the local coordinates (ξ, η) of P in E_t.

Figures 3(a) and (b) show the position of P in E_0 at time t_0 and in E_t at a later time t. Unless t is very close to t_0, P will not be in element E_0, but in an element E_t with lower number or even completely outside the network.

The number of element E_t and the local coordinates of P in E_t are calculated by the iterative procedure given below.

At time t the position of all nodes (x_n, y_n) is known from the solution of equations (1), (14) and (15) by the iterative procedure of the last section. Assume that P is in element E_k (which may be chosen as E_0) and solve equation (18) for (ξ, η), inserting the appropriate nodal

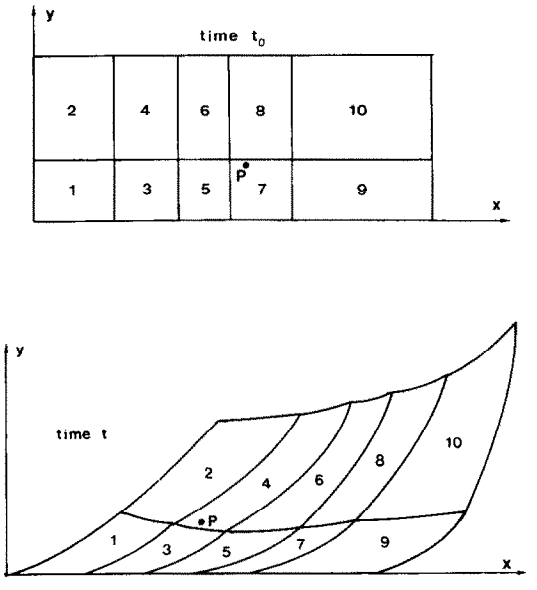

FIG. 3. Position of fixed point P in element 7 at time t_0 and in element 4 at time t.

point coordinates (x_n, y_n) for E_k in f_1 and f_2

$$f_1 = x - \sum_1^8 \phi_n(\xi, \eta) x_n = 0,$$
$$f_2 = y - \sum_1^8 \phi_n(\xi, \eta) y_n = 0. \tag{18}$$

Equation (18) is solved by Newton's method for $\boldsymbol{\theta} = (\xi, \eta)$

$$\boldsymbol{\theta} = \boldsymbol{\theta} - \left(\frac{\partial \mathbf{f}}{\partial \boldsymbol{\theta}}\right)^{-1} \mathbf{f} = \boldsymbol{\theta} - \mathbf{J}^{-\mathrm{T}} \mathbf{f}, \tag{19}$$

where $\mathbf{J}^{-\mathrm{T}}$ is the inverse of the transpose of the matrix defined in equation (A11).

If the solution $\boldsymbol{\theta}$ of equation (19) satisfies $-1 \leqslant \xi \leqslant 1$ and $-1 \leqslant \eta \leqslant 1$, P is located in E_k and the values of u, v and p at P can be found from equations (9)–(11). Moreover, if (ξ, η) are outside $[-1, 1]$ the actual values of ξ and η computed from equation (19) indicate in which element P is likely to be located. Thus, if $\xi = -3.4$ and $\eta = 1.8$, P is located to the left of and above E_k and the solution of equation (19) is repeated with another set of nodal point coordinates (x_n, y_n). We have found that the correct element is located in one or at most two iterations and now the solution of equation (19) yields the local coordinates of P.

With this location procedure one may calculate u and v for different values of y at a given set of x values—i.e. reconstruct a finite-element network with vertical parallel sides. Since equations (1)–(4) are solved by an initial value technique the integration may be restarted after a suitable rezoning procedure, and degeneracy of the elements is effectively avoided.

The simplest rezoning code would involve relocation of nodal points in the liquid to positions just below the surface nodal points. In Fig. 4 the new network is indicated by the broken lines between the open circles.

In the wave front the fluid particles experience a rapid deceleration and the surface nodes will approach each other. Hence, a rezoning procedure which is carried out after, e.g. every fifth time step will automatically give a finer network in the wave front where large deformations of the velocity field occur.

One would hesitate to carry out the rezoning too frequently since many equations (18) must be solved before the integration can be restarted. Consequently, the construction of an optimal rezoning procedure is of prime importance for the appropriate application of Lagrangian FEM simulation. We have persued this topic—but clearly the rate of change of the nodal point coordinates in the x-direction can be used to determine when rezoning is advisable.

A considerable improvement is, however, obtained by limiting the relative change of position of the surface nodes between two rezoning events. Assume that between time t_0 and t the surface nodes have moved as shown in Fig. 5 from the positions shown with full circles to positions shown with open circles. If the new network is constructed directly from the positions of the surface nodes at time t the film structure in front of the wave will be poorly represented because a very large element adjoins the slim elements in the wave front. Consequently, the surface nodes are rezoned as explained on Fig. 5 before the new nodal points in the interior of the liquid are constructed.

Let the elements be counted from the left on Fig. 5 by the index k, $k = 1, 2, \ldots, N_x - 1$, and let l_k be the length of the $\eta = 1$ edge of surface element k at time t. Furthermore, let the constant q be between 0 and 1.

We restrict the relative motion of the surface nodes by

$$q \leqslant \frac{l_{k+1}}{l_k} \leqslant \frac{1}{q}, \quad k = 1, 2, \ldots, N_x - 1. \tag{20}$$

If $q = 0$ no rezoning of surface nodes is made and if $q = 1$ the new surface nodes at time t will be placed equidistantly and one would not obtain the advantage of working with a finer network in the wave front.

Our numerical examples show that a q value of about 0.65 succeeds in collecting an appropriate number of nodal points in the wave front without extracting too many nodes from the upstream or downstream region of the film. A comparison between Figs. 7 and 8 clearly demonstrates the advantages of the improved rezoning procedure.

SIMULATION OF A WAVY LIQUID FILM

The solution of the wavy film problem offers a severe test of the FEM simulator, and it is a challenging problem since it has proved to be exceedingly difficult to solve in a rigorous fashion by other methods.

Some key results are summarized in Tables 1 and 2.

In each of the three examples the simulation has been carried out until there was no further change in the

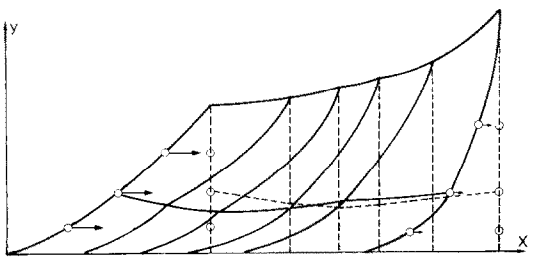

FIG. 4. Simple rezoning process.

FIG. 5. Improved rezoning process. ●, surface nodes of three consecutive elements after the previous rezoning event. ○, position of the same surface nodes just before the next rezoning event. One element side has become too large and two nodes are moved along the parabolic edge of the surface element to positions marked with arrows.

Table 1. Characterization of experimental system*

Example No.	Physical properties and operating parameters							
	ρ	μ	σ	Q	Re_N	h_N	$\langle u_N \rangle$	U_N
1	1.0	0.02	25	0.05	10	0.0145	3.45	5.17
2	1.0	0.072	40	0.9	50	0.0583	15.4	23.1
3	1.0	0.02	25	0.5	100	0.0312	16.0	24.0

* All quantities in cgs units.

wave form which is characterized by the shape factors h_{mx}, $2A$, L_b and L_f. These are defined in Fig. 6 (we use the same definitions as Dukler [10, Fig. 3]).

Values of the wave celerity c and of the shape factors are listed in Table 2. $N_x = 25$ was used in all examples and $q = 0.65$ was used in the 'improved' rezoning procedure.

In example 1 where Re_N is very small we have studied the influence of N_y and of the rezoning procedure on the accuracy of the simulated results.

The $N_y = 1$ simulation with no rezoning is very inaccurate, probably because a severe distortion of the elements has occurred before the stationary wave profile is reached.

When N_y is increased to 2 and a simple rezoning is applied one obtains approximately correct shape factors while the improved rezoning procedure provides a final correction to all quantities. No improvement is seen when N_y is increased to 3.

It is noted that the wave celerity c is relatively insensitive to improvements in the numerical method and consequently, the attainment of a simulated value for c that approximately fits an experimental value does not provide a severe test of the quality of the numerical method.

In example 2 we have used Nakorykov's data [4, p. 1014]. Nakorykov measured $c = 46$ cm s^{-1} and $h_{mx} = 0.112$ cm [4, Table 1]. The agreement with our simulated results is remarkable.

In example 3 the physical properties of the liquid are the same as in example 1, but the liquid flow has been increased by a factor 10 to give $Re_N = 100$.

There is a minor difference between values of c obtained with and without improvement of the rezoning procedure, but the shape factors of the wave change appreciably, just as was the case in the corresponding example with $Re_N = 10$.

Comparison of examples 1 and 3 shows that although c increases by a factor 2.7 when Re_N is increased from 10 to 100 the dimensionless celerity $c/\langle u_N \rangle$ actually decreases by a factor 1.7 to a value which is close to that measured by Brauner [2, Fig. 13] for $Re_N = 100$. The wave is much longer when $Re_N = 100$, but the length to amplitude ratio does not change significantly. $(L_b + L_f)/2A = 46$ for $Re_N = 10$ and 28 for $Re_N = 100$.

All the above simulations were started at t_0 with an initially equidistant, rectangular network and with $N_x = 25$. The distance between nodal points on the x-axis was 0.2 cm which means that the simulations cover a film of total length 5 cm. $h(x, t = t_0)$ was equal to the Nusselt film thickness h_N except that a perturbation in the shape of a Gaussian peak with height h_G and $2\sigma = B$ is superimposed on the elements close to $x = 0$.

In order to prove that the inlet perturbation has no influence on the final wave structure we have tried many different values of h_G/B. Thus, in example 3 ($h_G/h_N = 0.31$, $B/h_N = 33$) and ($h_G/h_N = 0.64$, $B/h_N = 33$) both gave exactly the same values as in Table 2. The stationary wave structure was reached in 3 min CPU time (on an IBM 4033 computer) in the first case while only 2 min was needed in the second case where the initial perturbation resembles the final large wave more closely. In example 2 we have tried to start with a perturbation as small as $h_G/h_N = 0.02$. Again, the same stationary wave (with $2A/h_N = 1.24$) is reached as when $h_G/h_N = 0.2$, but the computing time is considerably

Table 2. Main parameters for characterization of simulated wave structure*

Example No.	N_y	Rezoning	c	$c/\langle u_N \rangle$	$2A$	L_b	L_f	h_{mx}
	1	no	15.0	4.4	0.0074	1.11	0.60	0.0220
	1	simple	16.8	4.4	0.0098	0.96	0.30	0.0241
1	2	simple	19.2	5.6	0.0156	0.38	0.24	0.0296
	2	improved	18.1	5.2	0.0128	0.45	0.14	0.0275
	3	improved	18.0	5.2	0.0128	0.46	0.14	0.0276
2	2	improved	47.8	3.10	0.0720	1.10	0.31	0.1125
3	2	simple	49.0	3.06	0.0420	1.12	0.31	0.0693
	2	improved	49.4	3.09	0.0466	1.07	0.22	0.0710

* All quantities in cgs units.

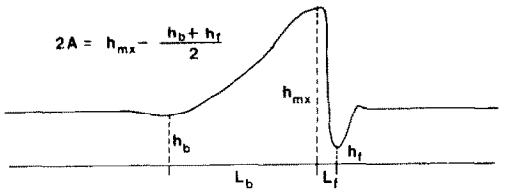

FIG. 6. Definition of shape parameters of the large wave.

longer. These calculations indicate that the smooth, vertically flowing film is unstable even to small perturbations, and also that the point of inception of the wave moves rapidly down the film when the perturbation becomes smaller. If we are interested only in the stationary wave there seems to be ample reason to start with a perturbation which resembles the final wave structure as closely as possible.

The evolution of the wave structure from the initially smooth film with an inlet disturbance closely resembles the experimental situation when a liquid flows over a weir to form a film which accelerates to a final velocity while it drains down a vertical wall. Hence it is reasonable to expect that a number of empirical correlations between c, shape factors, time of inception of waves and Re_N can be verified by the present numerical procedure.

The result of these comparisons will be reported elsewhere. In the present context we shall conclude our numerical examples by a presentation of some details concerning the wave form and we shall calculate u, v and p at different positions in the stationary wave.

Figure 7 shows the final (25 × 2) network from which the values of c and of the shape factors in example 2 were calculated. A characteristic feature is the deep trough which is being pushed down the film by the large wave. The steep forefront and much smoother receding front of the wave are features which are reported in numerous experimental studies, and we note a smaller, but clearly visible depression of the liquid surface behind the large wave. Ahead of the wave the Nusselt film thickness is h_N—in agreement with the condition which is imposed on the film outside the network. Far behind the large wave the Nusselt film thickness h_N is also reached—in agreement with the condition at $x = 0$ where fresh liquid is continuously fed with a parabolic velocity distribution.

The merits of the rezoning procedure are documented in Fig. 7. The forefront of the wave is represented by about ten elements and these are about ten times slimmer (0.02 cm) than the original elements. If the elements had not been allowed to shrink or expand we would have had to use ten times as many elements in the x-direction to obtain the same accuracy in the wave front calculations as in Fig. 7. From equation (17) this would imply an increase of the number N of equations to be solved in each integration step by a factor of almost ten (from 386 to 3761). This would again lead to an increase in computer time by a factor of at least $10N_y$, or 20 when $N_y = 2$.

Figure 8 is an enlarged view of the wave in example 2 computed with only the 'simple' rezoning procedure of Fig. 4. This may be compared with Fig. 7 (enlarged in Fig. 10 for the same x values as in Fig. 8) in which the improved rezoning was used. The main parameters c, h_{mx}, etc. are not very different whether they are obtained from Fig. 7 or from Fig. 8, but the fine structure of the film which precedes the wave is partially lost.

In Fig. 8 the wave front is represented by only two elements, and a very large element is just ahead of the small elements. In Fig. 7 there is a smooth transition from large elements far away from the wave to the thin elements in the wave front.

The improved rezoning procedure is even more beneficial in Fig. 9 which corresponds to example 3 with $Re_N = 100$. The damped 'forerunner' wave structure with amplitudes in the range of capillary waves is absent in Fig. 7, but is clearly visible at the higher value of Re_N in Fig. 9. The total length of the capillary wave structure is almost equal to that of the large wave and the trough between the two waves structures is even deeper in Fig. 9 than in Fig. 7. This is exactly what is seen on the

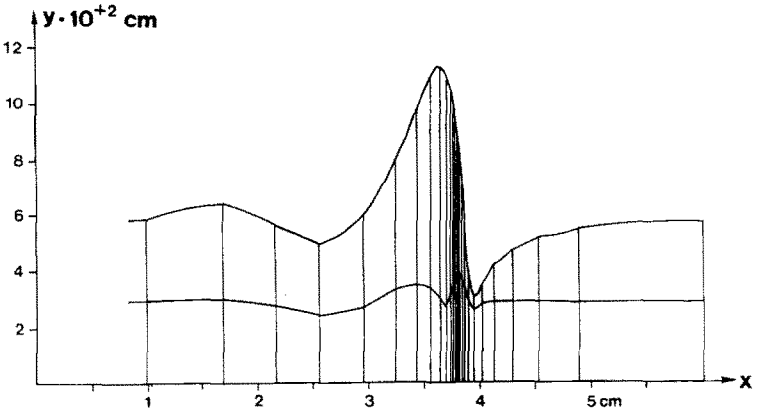

FIG. 7. Network and structure of wave after the stationary state has been reached. Parameters from example 2. Improved rezoning procedure.

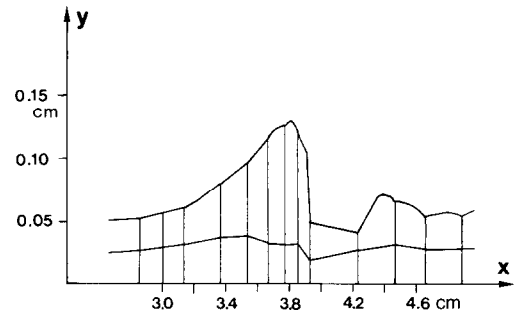

FIG. 8. Close-up view of the wave in example 2. The simple rezoning procedure has been used.

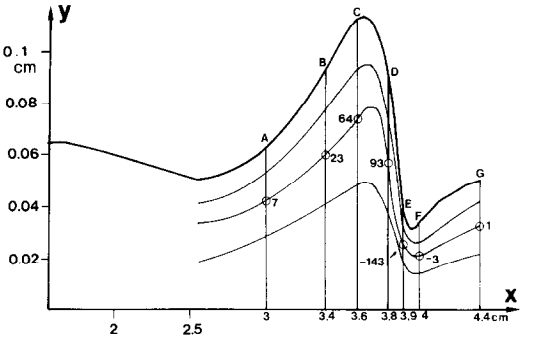

FIG. 10. Close-up view of the wave in example 2. Improved rezoning procedure. Three interior streamlines are shown. The pressure is shown (dyn cm^{-2}) at points marked with open circles, and velocities are reported in Table 3.

photographs in Kapitza [7, p. 708]: with $Re_N = 39$ there is no forerunner wave, but for $Re_N = 92$ there is clearly a capillary structure separated from the larger wave by a trough which goes almost to the bottom of the film.

The total length of the wave structure in Fig. 9 is so large that it might have been better to simulate more than 5 cm of the film ($N_x > 25$ or elements larger than 0.2 cm). No such refinements have been attempted, since the qualitative difference between Figs. 7 and 9 is clearly demonstrated with the present approximation.

In Fig. 10, an enlargement of the $3 < x < 4.4$ part of Fig. 7, three interior streamlines, corresponding to 0.25, 0.50, 0.75 of the total flow have been drawn, and in Table 3 values of u and v have been listed for the positions marked A–G on the figure. Also on Fig. 10 we have shown the value of p (dyn cm^{-2}) at selected positions marked with open circles. The pressure drops to -143 dyn cm^{-2} at position E, increases to ~ 100 dyn cm^{-2} in the wave front and returns slowly to zero after the wave.

The most remarkable feature of Fig. 10 and Table 3 is, however, the violent change in v which occurs just before the wave front. u and v are of the same order of magnitude and between $x = 3.95$ and 3.90, v changes from -3.5 to 7 cm s^{-1}. Since $u \sim 6$ cm s^{-1} the particle moves with a relative velocity $u' = u - c = -42$ cm s^{-1} against the wave, and the rapid change of v occurs in an extremely short time $\Delta t = \Delta x/(c-u) = 0.05/42 \cong 10^{-3}$ s. A fluid particle which is at a position quite close to the wall at $x = 3.95$ accelerates rapidly ($g' = (7+3.5)/10^{-3} \cong 10^4$ cm s^{-1}) out of the trough. It is swept towards the surface of the liquid and past the crest of the large wave before settling down in the smooth flow behind the wave. Clearly the mass transfer from the wall must be greatly enhanced in the region $3.85 < x < 3.9$. Brauner's figure [2, p. 103] and many previous experimental investigations, particularly by Dukler and coworkers, confirm that this is what happens in actual measurements of local mass transfer coefficients. From our simulations the wall shear stress, another experimentally measured quantity, can be calculated without any difficulty.

In the final Fig. 11 we compare values of u along the streamline on the receding part of the wave surface in

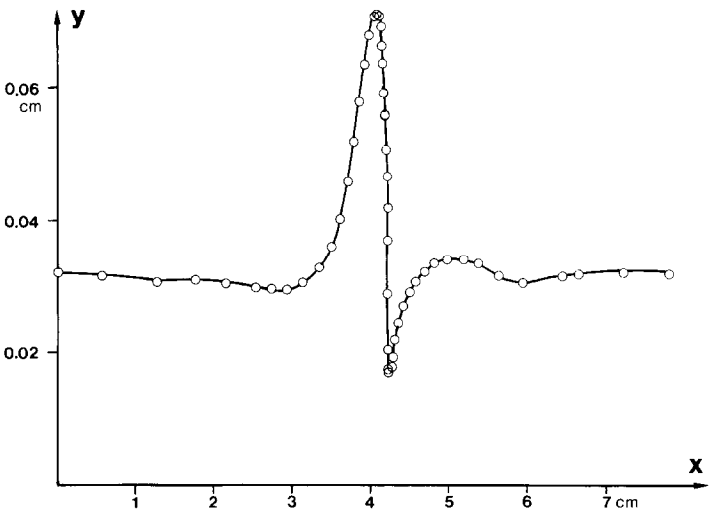

FIG. 9. Final wave structure for example 3.

Table 3. The velocity field in the region of the large wave*

Fluid path No.	Velocities (cm s^{-1}) at certain positions along paths 1–4													
	A		B		C		D		E		F		G	
	u	v	u	v	u	v	u	v	u	v	u	v	u	v
1†	31.6	−0.47	41.2	−0.04	41.4	1.05	33.9	1.36	9.8	7.22	12.7	−1.38	21.0	−0.08
2	30.6	−0.21	39.3	0.13	41.0	0.73	32.9	1.18	8.4	5.43	11.4	−1.00	20.3	−0.04
3	27.6	−0.10	35.3	0.20	37.4	0.43	30.0	0.90	7.0	3.36	9.8	−0.59	18.2	−0.01
4	21.6	−0.02	27.6	0.15	29.4	0.18	24.2	0.27	5.3	1.80	7.2	−0.32	13.9	~0

* All quantities in cgs units.
† Surface.

Fig. 7 with values computed from $h(x)$ by Nusselt's formula $U = (g\rho/2\mu)h^2$. It is quite obvious that the surface velocity is greatly overestimated if computed by Nusselt's formula. Consequently, any simulation of the wave structure which assumes a parabolic relation between u and $h(x)$ is qualitatively wrong. This is probably recognized by most investigators nowadays, but it has not always been so, as witnessed by a long list of early papers on wavy films which carry the erroneous assumption forward with no comments.

On Fig. 11 we have also shown Nakorykov's measurements [4, Fig. 3(a)]. There is again a remarkable coincidence between the experimental and simulated results.

CONCLUSION

In the present investigation we have constructed an FEM simulator and tested it on the classical problem of a wavy film which flows down a vertical wall. It has been proved that the method is able to find the stationary wave profile which develops on the film after a small perturbation is imposed on the smooth film at time t_0.

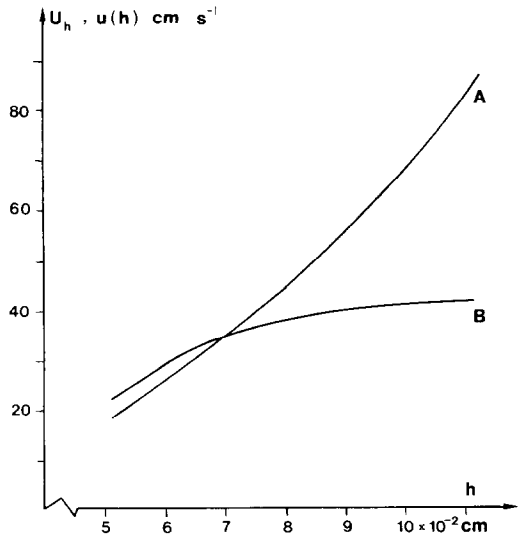

FIG. 11. Calculation of surface velocity by Nusselt's formula $U_h = (\rho g/2\mu)h^2$ (curve A) compared with the true velocity $u(y = h)$ (curve B).

Different parameters of the finite-element network have been varied to ascertain that sufficient accuracy could be obtained within a reasonable computing time. The final version of the simulator with an efficient rezoning procedure to rebuild the network when it has become distorted by the fluid motion is, indeed, quite fast, and stationary wave profiles are obtained in a matter of a few minutes CPU time on an IBM 3033 computer.

Although we have made some comparisons of calculated results with experimental values and found excellent agreement between the two, one should in fact carry out many more calculations in order to obtain correlations between, e.g. the shape factors of the wave and the properties of the liquid phase or the operation conditions (in terms of Re_N). Once the velocity field in waves of different shape has been obtained, one could proceed to calculate the solution of the 2-D mass balances for a liquid component which is transported from the wall to the free surface or vice versa.

REFERENCES

1. P. Bach and O. Hassager, A Lagrangian finite element method for the simulation of flow of Newtonian liquids, *A.I.Ch.E. Jl* (1984) in press.
2. N. Brauner and D. M. Maron, Characteristics of inclined thin films. Waviness and the associated mass transfer, *Int. J. Heat Mass. Transfer* **25,** 99–110 (1982).
3. W. J. Strobel and S. Whitaker, The effect of surfactants on the flow characteristics of falling liquid films, *A.I.Ch.E. Jl* **15,** 527–532 (1969).
4. V. E. Nakorykov, B. G. Pokusaev, S. V. Alekseenko and V. V. Orlov, Instantaneous velocities in a wavy fluid film, *J. Engr Phys.* **33,** 1012–1016 (1977) (English translation).
5. V. E. Nakorykov, B. G. Pokusaev and S. V. Alekseenko, Stationary rolling waves on a vertical film of liquid, *J. Engr Phys.* **30,** 517–521 (1976) (English translation).
6. F. W. Pierson and S. Whitaker, Some theoretical and experimental observations of the wave structure of falling films, *Ind. Engng Chem. Fundam.* **16,** 401–408 (1977).
7. P. L. Kapitza, Wave flow of thin layers of a viscous fluid, *Collected Papers of P. L. Kapitza*, Vol. II. Macmillan, New York (1964).
8. A. S. Telles and A. E. Dukler, Statistical characteristics of thin, vertical wavy liquid films (part I), *Ind. Engng Chem. Fundam.* **9,** 412–421 (1970).
9. K. J. Chu and A. E. Dukler, Statistical characteristics of thin, wavy films (part II), *A.I.Ch.E. Jl* **20,** 695–706 (1974).
10. K. J. Chu and A. E. Dukler, Statistical characteristics of thin, wavy films (part III), *A.I.Ch.E. Jl* **21,** 583–593 (1975).

11. H. Lamb, *Hydrodynamics* (6th edn.). Cambridge University Press, London (1945).
12. J. J. Connor and C. A. Brebbia, *Finite Element Techniques for Fluid Flow*. Butterworths, London (1976).
13. T. J. Chung, *Finite Element Analysis in Fluid Dynamics*. McGraw Hill, New York (1978).
14. R. L. Sani, P. M. Gresho, R. L. Lee and D. F. Griffiths, The cause and cure (?) of the spurious pressures generated by certain FEM solutions of the incompressible Navier–Stokes equations, parts 1 and 2, *Int. J. Num. Methods Fluids* **1**, 17–43 and 171–204 (1981).
15. R. B. Bird, E. N. Lightfoot and W. E. Stewart, *Transport Phenomena*. Wiley, New York (1960).
16. P. Bach, M.Sc. thesis (in Danish), Instituttet for Kemiteknik, DTH (1982).
17. A. E. Dukler, Characterization, effects and modeling of the wavy gas–liquid interface, *Progr. Heat Mass Transfer* **6**, 207–223 (1972).
18. W. J. Silliman and L. E. Scriven, Separating flow near a static contact line: slip at a wall and shape of a free surface, *J. Comp. Phys.* **30**, 287–313 (1980).
19. K. J. Ruschak, A method for incorporating free boundaries with surface tension in finite element fluid-flow simulators, *Int. J. Num. Methods Engng* **15**, 639–648 (1980).
20. C. S. Frederiksen and A. M. Watts, Finite element method for time dependent incompressible free surface flow, *J. Comp. Phys.* **39**, 282–304 (1981).
21. O. Hassager and C. Bisgaard, A Lagrangian finite element method for the simulation of flow of non-Newtonian liquids, *J. Non-Newtonian Fluid Mech.* **12**, 153–164 (1983).
22. J. T. Oden and L. C. Wellford, Jr., Analysis of flow of viscous fluids by the finite element method, *AIAA J.* **10**, 1590–1599 (1972).

APPENDIX

INTERPOLATION POLYNOMIALS AND GALERKIN MATRICES

The interpolation functions $\phi_n(\xi,\eta)$ and $\psi_n(\xi,\eta)$ which are used to approximate u, v and p inside the element are taken from [13, p. 83]

$$\psi_n(\xi,\eta) = \tfrac{1}{4}(1+\xi_n\xi)(1+\eta_n\eta), \tag{A1}$$

where

$$(\xi_n,\eta_n) = (-1,-1),(1,-1),(1,1) \quad \text{and} \quad (-1,1) \qquad \text{for} \quad n = 1,2,3,4,$$

$$\phi_n(\xi,\eta) = \tfrac{1}{4}(1+\xi_n\xi)(1+\eta_n\eta)(\xi_n\xi+\eta_n\eta-1) \qquad \text{for} \quad n = 1,3,5 \text{ and } 7,$$

and

$$\tfrac{1}{2}(1-\xi^2)(1+\eta_n\eta) \qquad \text{for} \quad n = 2,6, \tag{A2}$$

and

$$\tfrac{1}{2}(1+\xi_n\xi)(1-\eta^2) \qquad \text{for} \quad n = 4,8.$$

The nodal points are numbered according to Fig. 2(a).

In the following list of the elements of **A**, **C**, **D**, **E** and **F** it is sometimes convenient to order the components of the velocity vector as **V** in equation (A3) and sometimes as $\mathbf{V}_1$ in equation (A4). Before inserting the results into equations (14) and (15) one must reorder the rows of all quantities to conform with the ordering shown in **V**

$$\mathbf{V} = (u_1, u_2, \ldots, u_8, v_1, v_2, \ldots, v_8), \tag{A3}$$

$$\mathbf{V}_1 = (u_1, v_1, u_2, v_2, \ldots, u_8, v_8). \tag{A4}$$

The dissipation matrix **D**. *Velocities ordered as* $\mathbf{V}_1$

$$\mathbf{D} = \mu \begin{pmatrix} d_{11} & d_{12} & \cdots & d_{18} \\ \vdots & \vdots & \vdots & \vdots \\ d_{81} & d_{82} & \cdots & d_{88} \end{pmatrix}, \tag{A5}$$

where

$$d_{ij} = \begin{pmatrix} \delta_{11} & \delta_{12} \\ \delta_{21} & \delta_{22} \end{pmatrix}, \tag{A6}$$

and

$$\delta_{11} = \int_\Omega \left(2\frac{\partial\phi_i}{\partial x}\frac{\partial\phi_j}{\partial x} + \frac{\partial\phi_i}{\partial y}\frac{\partial\phi_j}{\partial y} \right) \mathrm{d}\Omega, \tag{A7}$$

$$\delta_{22} = \int_\Omega \left(2\frac{\partial\phi_i}{\partial y}\frac{\partial\phi_j}{\partial y} + \frac{\partial\phi_i}{\partial x}\frac{\partial\phi_j}{\partial x} \right) \mathrm{d}\Omega, \tag{A8}$$

$$\delta_{12} = \int_\Omega \frac{\partial\phi_i}{\partial x}\frac{\partial\phi_j}{\partial y}\,\mathrm{d}\Omega, \tag{A9}$$

$$\delta_{21} = \int_\Omega \frac{\partial\phi_j}{\partial x}\frac{\partial\phi_i}{\partial y}\,\mathrm{d}\Omega. \tag{A10}$$

In **D** as well as in the other quantities to be determined here one must compute the derivatives of the interpolation functions with respect to x and y

$$\begin{aligned} \begin{pmatrix} \frac{\partial}{\partial\xi}\phi_n \\ \frac{\partial}{\partial\eta}\phi_n \end{pmatrix} &= \begin{pmatrix} \frac{\partial x}{\partial\xi}\frac{\partial y}{\partial\xi} \\ \frac{\partial x}{\partial\eta}\frac{\partial y}{\partial\eta} \end{pmatrix} \begin{pmatrix} \frac{\partial}{\partial x}\phi_n \\ \frac{\partial}{\partial y}\phi_n \end{pmatrix} \\ &= \begin{pmatrix} \sum\frac{\partial\phi_i}{\partial\xi}x_i & \sum\frac{\partial\phi_i}{\partial\xi}y_i \\ \sum\frac{\partial\phi_i}{\partial\eta}x_i & \sum\frac{\partial\phi_i}{\partial\eta}y_i \end{pmatrix} \begin{pmatrix} \frac{\partial\phi_n}{\partial x} \\ \frac{\partial\phi_n}{\partial y} \end{pmatrix} \\ &= \mathbf{J} \begin{pmatrix} \frac{\partial\phi_n}{\partial x} \\ \frac{\partial\phi_n}{\partial y} \end{pmatrix}, \end{aligned} \tag{A11}$$

$$\begin{pmatrix} \frac{\partial\phi_n}{\partial x} \\ \frac{\partial\phi_n}{\partial y} \end{pmatrix} = \mathbf{J}^{-1} \begin{pmatrix} \frac{\partial\phi_n}{\partial\xi} \\ \frac{\partial\phi_n}{\partial\eta} \end{pmatrix}. \tag{A12}$$

The summations are from $i = 1$ to 8 and the partial derivatives of ϕ_n ($n = 1,2,\ldots,8$) with respect to ξ and η are easily found from equation (A2).

In equations (A7)–(A10) a number of integrals over the element area Ω are computed

$$\mathrm{d}\Omega = \mathrm{d}x\,\mathrm{d}y = \det(\mathbf{J})\,\mathrm{d}\xi\,\mathrm{d}\eta, \tag{A13}$$

$$\int_\Omega f\,\mathrm{d}\Omega = \int_{-1}^{1}\int_{-1}^{1} f\left(\phi_n, \frac{\partial\phi_n}{\partial x}, \frac{\partial\phi_n}{\partial y}\right) \det(\mathbf{J})\,\mathrm{d}\xi\,\mathrm{d}\eta. \tag{A14}$$

All integrals are calculated by three-point Gauss quadrature (quadrature points $\pm(3/5)^{1/2}$ and 0). This is straightforward in **A**, **D**, **E** and **F** while the calculation of elements in **C** requires some special consideration.

The inertia matrix **A**. *Velocities ordered as* **V**

$$\mathbf{A} = \rho \begin{pmatrix} \mathbf{A}_1 & 0 \\ 0 & \mathbf{A}_1 \end{pmatrix}, \tag{A15}$$

where the (8×8) matrix $\mathbf{A}_1$ is given by

$$A_{ij} = \int_\Omega \phi_i \phi_j \, d\Omega. \tag{A16}$$

The pressure matrix **C**. *Velocities ordered as* $\mathbf{V}_1$

$$\mathbf{C} = \begin{pmatrix} \mathbf{C}_1 \\ \mathbf{C}_2 \\ \vdots \\ \mathbf{C}_8 \end{pmatrix}, \tag{A17}$$

where $\mathbf{C}_j$ is a (2×4) matrix with elements $(C_j)_{km}$ given by

$$\begin{aligned} (C_j)_{km} &= \int_\Omega \psi_m \frac{\partial \phi_j}{\partial x} \, d\Omega \quad \text{for} \quad k = 1, \\ (C_j)_{km} &= \int_\Omega \psi_m \frac{\partial \phi_j}{\partial y} \, d\Omega \quad \text{for} \quad k = 2. \end{aligned} \tag{A18}$$

The integrals in equation (A18) are taken over the area Ω of the quadratic element, but the pressure field is defined on a bilinear element, and in general the set of local coordinates (ξ', η') of any particular Gauss quadrature point P in the bilinear element is not the same as the local coordinates (ξ, η) of P in the quadratic element. Thus, in order to avoid errors in equation (A18) where the function f in equation (A14) contains ψ_n besides $\partial\phi_n/\partial x$ and $\partial\phi_n/\partial y$ one must compute the correct argument (ξ', η') in ψ by solution of the non-linear equations

$$x_i = \boldsymbol{\psi}^{\mathrm{T}}(\xi', \eta')\mathbf{x}_i = \tfrac{1}{4}(1, \xi', \eta', \xi'\eta') \times \begin{pmatrix} 1 & 1 & 1 & 1 \\ -1 & 1 & 1 & -1 \\ -1 & -1 & 1 & 1 \\ 1 & -1 & 1 & -1 \end{pmatrix} \mathbf{x}_i, \tag{A19}$$

where x_i $(i = 1, 2)$ are the coordinates (x, y) of the quadrature point P in Ω and $\mathbf{x}_i$ is the vector of nodal point coordinates (x_n, y_n), $n = 1, 2, 3, 4$ in the bilinear element.

The problem of finding (ξ', η') in equation (A19) is the same as that of finding (ξ, η) for a given (x, y) in the location problem (18), but rather than using Newton's method to solve equation (A19) we have preferred to reformulate equation (A19) into a quadratic equation which may be solved explicitly for (ξ', η') [16].

If it happens that the midpoint nodes 2, 4, 6 and 8 of the quadratic element fall on the straight lines between the corners of the element then (ξ', η') is exactly equal to (ξ, η), and the same Gaussian points may be used to calculate **C** and the other matrices. Silliman and Scriven [18] who used the same order of the finite elements as we have used took $(\xi', \eta') = (\xi, \eta)$ without any comments, but we believe our procedure is more correct since the properties of the quadratic element are more fully exploited to give a better approximation for the unknowns.

Mass force vector **F**. *Velocities ordered as* **V**

$$\begin{aligned} F_j &= g \int_\Omega \phi_j \, d\Omega \quad \text{for} \quad j = 1, 2, \ldots, 8, \\ F_j &= 0 \qquad\qquad \text{for} \quad j = 9, 10, \ldots, 16. \end{aligned}$$

Surface force vector **E**. *Velocities ordered as* **V**

Surface terms appear only in elements which adjoin the free surface. We have used Gauss–Green's theorem to convert the 2-D integral into a line integral, substituting the RHS of equation (6) for the sum of the two terms on the LHS. This procedure is also described in Chung [13, p. 207]

$$\mathbf{E} = \begin{pmatrix} \mathbf{E}_1 \\ \mathbf{E}_2 \end{pmatrix}$$

where

$$\mathbf{E}_1 = \begin{pmatrix} e_{11} \\ \vdots \\ e_{18} \end{pmatrix}$$

and

$$\mathbf{E}_2 = \begin{pmatrix} e_{21} \\ \vdots \\ e_{28} \end{pmatrix}, \tag{A20}$$

$$\begin{aligned} e_{1j} &= -\int_{-1}^{1} \phi_j(s) 2H\sigma \frac{\partial y}{\partial s} \, ds, \\ e_{2j} &= \int_{-1}^{1} \phi_j(s) 2H\sigma \frac{\partial x}{\partial s} \, ds, \end{aligned} \tag{A21}$$

$$\begin{aligned} \phi_j(s) &= \phi_j(\xi = s, \eta = 1), \\ \frac{\partial x}{\partial s} &= \sum_1^8 \frac{d\phi_k(s)}{ds} x_k, \quad \frac{\partial y}{\partial s} = \sum_1^8 \frac{d\phi_k(s)}{ds} y_k. \end{aligned} \tag{A22}$$

H can be calculated from the interpolation functions ϕ_n if these are at least quadratic (otherwise $\partial^2 h/\partial x^2 = 0$).

The three interpolation functions ϕ_n which are used on the surface have indices 7, 6 and 5 [see Fig. 2(a)]. Hence, with $j = 8 - n$, $n = 7, 6, 5$:

	$j = 1$	$j = 2$	$j = 3$
$\phi_j(s)$	$-\frac{1}{2}s(1-s)$	$1-s^2$	$\frac{1}{2}s(1+s)$
$\dfrac{d\phi_j}{ds}$	$s-\frac{1}{2}$	$-2s$	$s+\frac{1}{2}$
$\dfrac{d^2\phi_j}{ds^2}$	1	-2	1

$$\begin{aligned} \frac{\partial h}{\partial x} &= \frac{\partial h}{\partial s}\frac{\partial s}{\partial x} = \left(\sum_1^3 \frac{d\phi_j(s)}{ds} y_j\right)\frac{\partial s}{\partial x}, \\ \frac{\partial^2 h}{\partial x^2} &= \frac{\partial}{\partial x}\frac{\partial h}{\partial x} = \left(\sum_1^3 \frac{d^2\phi_j(s)}{ds^2} y_j\right)\left(\frac{\partial s}{\partial x}\right)^2 \\ &= (y_7 - 2y_6 + y_5)\left(\frac{\partial s}{\partial x}\right)^2, \end{aligned} \tag{A23}$$

and finally

$$\frac{\partial s}{\partial x} = \left(\sum_1^3 \frac{d\phi_j}{ds} x_j\right)^{-1}. \tag{A24}$$

Silliman and Scriven [18] claim that it is too inaccurate to calculate $2H$ from the derivatives of the interpolation functions as we have done. They prefer to approximate the surface by a circular arc through three consecutive points A, B and C on the surface. Next, by Heron's formula they obtain

$$|2H| = \frac{(4d(d-a)(d-b)(d-c))^{1/2}}{abc}, \tag{A25}$$

where a, b and c are the lengths of chords between A and B, B and C, and C and A, respectively, $d = \frac{1}{2}(a+b+c)$.

Numerical calculations of H for several curved surfaces of known shape have shown that our method gives virtually the same results as Silliman and Scriven's procedure—and it is also hard to see any major difference between the two methods.

Ruschak [19] was probably the first to include the effect of surface tension in an FEM simulation of a free surface flow problem. He used bilinear elements for the velocity field (and accordingly he assumed the pressure to be constant within the element), and he had to give his free surface elements some curious 'extra degrees of freedom' to be able to include the effect of surface tension. Silliman and Scriven's method [18] could presumably be used for bilinear as well as for quadratic elements, but when we tried to do so in some preliminary calculations very disappointing results were obtained: the surface had a saw tooth character and chequerboarding of the pressure field developed. No such phenomena were ever observed when quadratic finite elements were used.

SIMULATION DE L'ECOULEMENT VERTICAL D'UN FILM MINCE ET ONDULE, PAR UNE METHODE AUX ELEMENTS FINIS

Résumé—Les équations de Navier–Stokes pour un film liquide bidimensionnel qui descend le long d'une paroi verticale en écoulement laminaire, sont formulées en fonction des vitesses lagrangiennes et elles sont résolues par une méthode aux éléments finis. Un excellent accord est obtenu entre les calculs de la célérité et de la forme de l'onde et les résultats expérimentaux. Les bilans de quantité de mouvement et de masse, discrétisés en fonction des valeurs aux noeuds pour la vitesse et la pression, sont résolus par la méthode de Galerkin. Pour éviter la distortion du réseau dans l'accroissement du temps d'intégration, on utilise une procédure de zonage adaptable. Ceci maitrise un défaut de la formulation lagrangienne et permet la poursuite de l'intégration jusqu'à l'obtention d'un profil stationnaire.

SIMULATION DER SENKRECHTEN STRÖMUNG EINES DÜNNEN, WELLIGEN FILMS MIT HILFE DER METHODE DER FINITEN ELEMENTE

Zusammenfassung—Für einen zweidimensionalen Flüssigkeitsfilm, der in laminarer Strömung an einer senkrechten Wand herabfließt, werden mit Hilfe der Lagrange'schen Geschwindigkeiten die Navier–Stokes-Gleichungen formuliert und nach dem Verfahren der finiten Elemente gelöst. Zwischen den berechneten Resultaten für Wellengeschwindigkeit und -form und den entsprechenden experimentellen Ergebnissen besteht vorzügliche Übereinstimmung. Die Bilanzen für Impuls- und Stofftransport, die mit Hilfe der Knotenpunkts-Werte für Geschwindigkeit und Druck diskretisiert sind, werden mit der Methode von Galerkin gelöst. Um bei wachsender Integrationszeit eine Gitterverzerrung zu vermeiden, wurde ein Verfahren zur Neueinteilung des Gitters entwickelt, das den Hauptmangel bei der Lagrange'schen Formulierung überwindet und es erlaubt, die Integration fortzusetzen, bis ein stationäres Wellenprofil erreicht ist.

МОДЕЛИРОВАНИЕ ВЕРТИКАЛЬНОГО ТЕЧЕНИЯ ТОНКОЙ ВОЛНООБРАЗНОЙ ПЛЕНКИ МЕТОДОМ КОНЕЧНЫХ ЭЛЕМЕНТОВ

Аннотация—Уравнения Навье–Стокса для двумерной пленки жидкости, ламинарно стекающей по вертикальной стенке, формулируются через скорости Лагранжа и решаются методом конечных элементов. Получено хорошее совпадение между разультатами моделирования скорости стекания пленки и ее формы и соответствующими экспериментальными данными. Балансы количества движения и массы, выраженные в дискретном виде через значения скорости и давления в узловых точках, решаются методом Галеркина. Разработана специальная методика для предотвращения деформации расчетной сетки при возрастающих временах интегрирования. Это позволяет сгладить основной недостаток формулировки Лагранжа и проводить интегрирование вплоть до достижения стационарного волнового профиля пленки.